Research Article | Vol. 34, No. 17 / 24 Aug 2026 / Optics Express 30973
Optics EXPRESS

Rapid mechanical scanning at 8 kHz for in-flow mid-IR field-resolved spectroscopy

LORENZO GATTO,[1,*] WOLFGANG SCHWEINBERGER,[2,3] MARINUS HUBER,[2,4] YUAN SI,[2] ZHENG WEI,[1,2] SEBASTIAN GRÖBMEYER,[2] CSABA LIBER,[3] FRANK FLEISCHMANN,[2] IOACHIM PUPEZA,[4,5,6,7] ALEXANDER WEIGEL,[1,2,3] AND MIHAELA ŽIGMAN[1,2,8]

[1]*Max Planck Institute of Quantum Optics (MPQ), Garching, Germany*
[2]*Chair of Experimental Physics - Laser Physics, Faculty of Physics, Ludwig-Maximilians-Universität München (LMU), Garching, Germany*
[3]*Center for Molecular Fingerprinting (CMF), Frontiers Foundation, Budapest, Hungary*
[4]*Leibniz Institute of Photonic Technology (IPHT), Jena, Germany*
[5]*Physics Department and State Research Center OPTIMAS, University of Kaiserslautern-Landau, Kaiserslautern, Germany*
[6]*Cluster of Excellence Balance of the Microverse, Friedrich Schiller University Jena, Jena, Germany*
[7]*Fraunhofer Institute for Industrial Mathematics ITWM, Kaiserslautern, Germany*
[8]*Institute of Pathology, Faculty of Medicine, Ludwig-Maximilians-Universität München (LMU), Munich, Germany*
[*]*lorenzo.gatto@mpq.mpg.de*

Abstract: High-speed vibrational spectroscopy is a sensitive label-free approach for molecular fingerprinting in dynamic and non-repetitive systems. Field-resolved mid-IR spectroscopy based on electro-optic sampling (EOS) offers broad bandwidth and high dynamic range, but reducing the technical complexity of high-speed implementations remains challenging. Here, we demonstrate the use of a galvanometer scanner resonant at 4 kHz for high-speed EOS of mid-IR pulses with a single-scan acquisition time of 125 µs. Interferometric delay tracking and reconstruction provide femtosecond-level timing precision and spectra compatible with those of conventional slow-scan, lock-in measurements. We validate the operational functionality of the EOS resonant scanner by monitoring dimethyl sulfone concentration in water in a flow-through cuvette in real time. This approach offers advantages in reducing technical complexity, improving cost-effectiveness, and enabling flexible selection of the scanning speed.

1. Introduction

High-speed delay-scanning methods, in parallel with new fast-detection techniques, have been expanding the capabilities of vibrational spectroscopy. Stroboscopic and step-scan time-resolved Fourier transform infrared (FTIR) spectroscopy extended broadband infrared spectroscopy into the regime of sub-millisecond dynamics, achieving microsecond or even nanosecond resolution [1,2]. These techniques can capture repetitive or cyclic processes, in which the system's equilibrium state can be easily restored, and the response replicated identically or with negligible variations upon a new trigger event [3,4].

However, many chemical processes of interest and spectroscopy applications are not intrinsically repetitive. For example, caged-compound-induced reactions [5], as well as micro-particles or biological cells' fingerprinting in flow [6–8], and fast referencing measurements [9]. In these cases, the single-scan acquisition time becomes a decisive performance parameter and must be shorter than the fastest relevant time scale of the process under investigation. Advances in

#607523 https://doi.org/10.1364/OE.607523
Journal © 2026 Received 10 Jun 2026; revised 15 Jul 2026; accepted 25 Jul 2026; published 10 Aug 2026

Optics EXPRESS

laser-based mid-infrared (mid-IR) sources [10] have facilitated high-speed delay scanning via two main strategies: repetition-rate control and frequency upconversion [11].

The first strategy is used in asynchronous optical sampling (ASOPS) [12] and dual-comb spectroscopy (DCS), promoting new advances in metrology [13,14]. Although spectral resolution and bandwidth are often prioritized in the field of DCS [15–17], they can also be traded off against the acquisition speed, typically using repetition rates in the GHz range [4,18,19]. Dephasing often occurs on the picosecond time scale (e.g., liquid-phase spectroscopy), and the delay range of ASOPS or DCS results in the acquisition of many unnecessary data points. Electronically controlled optical sampling (ECOPS) [20] can be adopted to restrict the delay range without resorting to very short cavities. Methods based on repetition rate control can thus achieve multi-kHz scanning rates.

Frequency upconversion transfers information from the mid-IR to the near-IR or visible range, where sensors with faster response times and better noise figures can be used. This principle has enabled new fast FTIR spectrometers [21] and spectroscopic techniques with measurement rates beyond MHz [22]. Near-IR photodetectors (e.g., InGaAs-based) can operate at bandwidths even three orders of magnitude higher than those of conventional mid-IR detectors, such as HgCdTe (MCT). Upconversion methods can therefore achieve a 1000-fold increase in scanning speed ($\sim$ delay window length $\times$ scan rate) compared to conventional FTIR spectrometers, without sacrificing spectral resolution. Quantum cascade detectors can achieve electrical bandwidths of the order of 10 GHz, with a tunable detection wavelength. Nevertheless, due to the limited spectral coverage of the single detectors, they have been predominantly used for relatively narrowband applications so far [23,24].

In electro-optic sampling (EOS), the electric field of an infrared pulse is sampled in the time domain through its nonlinear interaction with a shorter near-infrared gate pulse within a crystal [25–27]. In the simplest implementations, the delay between the two pulses is scanned with a motorized translation stage. EOS can be viewed as an upconversion-based technique, in which the information carried by the mid-IR waveform is encoded in the polarization of the near-IR gate. As such, it has in principle the same advantages as upconversion in terms of scanning speed. Furthermore, EOS inherently implements a self- heterodyne/homodyne detection concept [27,28] and combines it with balanced photodetection. Its characteristics inherently support high-dynamic-range measurements of electric-field oscillations, with broad spectral coverage and high signal-to-noise ratio. Mid-IR field-resolved spectroscopy (FRS) [29] offers a distinct advantage in aqueous environments: because the detected response scales with the electric field rather than intensity, weak molecular signatures can be retrieved with enhanced sensitivity in the presence of strong water absorption [30]. This capability is especially relevant for studying the dynamics of biomolecules under physiological conditions.

Rapid-scanning EOS offers several advantages over the traditional combination of slow-scanning delay stages and lock-in or boxcar detection [31]. While slow-scanning methods remain widespread due to their simplicity and reliability, rapid-scanning modalities suppress low-frequency noise components within a single scan and allow for fast referencing with minimal spectral distortion. Repetition-rate control has been applied to increase the mid-IR EOS scanning rate [32,33].

Single-shot EOS methods have been extensively developed in the THz range (f $\sim$ 1-10 THz) [34]. Although some of the available techniques have already been extended to mid-IR pulses [35,36], their broader application in the mid-IR, however, remains technically demanding because frequency-to-time or space-to-time mapping can introduce waveform distortions that require careful consideration [34].

Acousto-optic programmable dispersive filters (AOPDF) provide another non-mechanical route to rapid delay scanning and have been used for THz time-domain spectroscopy at 36 kHz scan rates [37]. The main technical challenges, however, are the limited diffraction efficiency,

Optics EXPRESS

which reduces the gate beam energy, and the handling of dispersion when using ultrabroadband pulses.

Overall, high-speed mid-IR FRS implementations can deliver exceptional scan rates, waveform stability, resolution, and bandwidth. Nevertheless, to achieve such performance, they usually require expensive specialized hardware and complex electronic locking systems. Rapid mechanical delay scanning offers a complementary compromise: although it typically achieves lower scan rates [38], it can be implemented with relatively simple, cost-effective instrumentation.

In conventional mechanical delay lines, fast linear motion is commonly achieved using voice-coil or piezo actuators. As can be understood considering a simple harmonic oscillator, the force required to invert the actuator's motion is proportional to the square of the scanning frequency and to the mass of the reflector assembly. This typically limits the scan rate below 1 kHz for the commonly available linear actuators [3,38]. Higher scanning speeds can be achieved by amplifying ultrasonic piezo motion with a sonotrode, reaching 38 kHz [39,40]. However, this approach also requires bulky, relatively expensive hardware.

Rotating optical elements avoid the reversal of the motion at the end of the travel range and are therefore implemented in rapid-scanning FTIR concepts [3]. Similar approaches have also been adapted for FRS, especially in the THz range [41–43]. Oscillating optical elements provide a related strategy. In particular, the low inertia and resonant operation of galvanometer scanners, characterized by large oscillation amplitude and stability, are interesting characteristics when building platforms for rapid delay scanning. An all-reflective optical delay line combining a resonant scanner with a retro-reflecting 4f-telescope was originally introduced for optical coherence tomography [44] and later adapted to various rapid-scanning spectroscopic applications [7,45]. To our knowledge, however, this concept has not yet been applied to field-resolved spectroscopy.

Here, we implement a modified version of the design described in [44] for rapid-scanning EOS of mid-IR pulses. This rapid delay line, with a small footprint, requires only one mode-locked laser and no additional high-performance electronics for active cavity-length stabilization. Furthermore, the approach is compatible with broadband pulses and allows flexible selection of the scanning rate. As a proof-of-principle, we demonstrate real-time chemical detection in a dynamic aqueous environment by monitoring the concentration of a model molecule in a flow-through cuvette.

2. Methods

Mid-IR pulses are obtained by intrapulse difference frequency generation (IPDFG) in a lithium gallium sulfide (LGS) crystal, pumped by ultrashort pulses at 11 MHz repetition rate and 1030 nm central wavelength provided by an Yb:YAG thin-disk oscillator. A fraction of the residual driving laser after the IPDFG is used as a gate pulse for EOS.

We used a resonant galvanometer scanner oscillating at 4 kHz (EOP-SC-30, Laser 2000 GmbH, mirror size: 8 mm x 9 mm. Oscillating mirror (OM) in Fig. 1(a)) to rapidly modulate the delay between the gate and the mid-IR. A folded 4f-telescope (comprising a concave mirror (CM) f=50 mm and D-shaped mirror (DM), see Fig. 1(a)) compensates for the angular deviation of the gate beam, so that the output of the rapid delay line can be used for EOS.

In the experimental setup described in Ref. [44], the concave mirror and the retroreflector were placed in the same horizontal plane where the oscillation of the galvanometer was taking place. The apex of the concave mirror and its horizontal tilt were then adjusted, together with the tilt of the retroreflector, to minimize the fluctuations of the output beam. Here, instead, the D-shaped retroreflector is placed just above the resonant scanner mirror to minimize the angular deviations. The D shape allows the retroreflector to be placed almost in contact with the upper edge of the resonant scanning mirror while using its clear aperture efficiently. This means that the CM has to vertically displace the beam by just 1-3^o, and the DM has to be vertically tilted

Optics EXPRESS

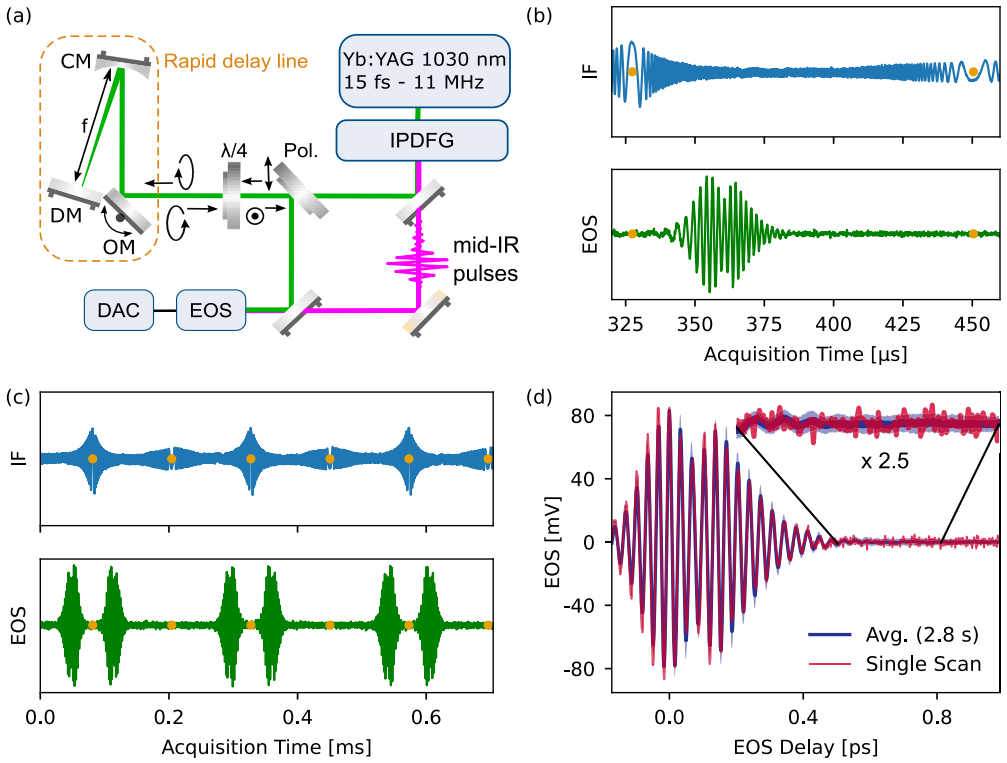

Fig. 1. (a) Schematic representation of the experimental setup. The rapid-scanning delay line comprises an oscillating mirror (OM) mounted on the scanner, resonant at 4 kHz, a concave mirror (CM, f = 50 mm), and a D-shaped mirror (DM), laterally displaced for easier visualization but in reality just above OM. (b) Example of the raw data before delay extraction. The top and bottom panels represent the interferogram (IF) and the EOS signal, respectively. The orange dots are the scanning turning points automatically detected by the data processing algorithm. (c) Extended raw data acquisition showing forward and backward scans. (d) Single scan (red) and time-domain-averaged scan (blue), showing the acquisition stability. The shaded error bar (blue) shows the standard deviation of the single scans over 2.8 s (single scan noise).

by the same amount to send the beam back to the original direction. One consequence of this modified design is that the angular deviations required to fold the beam path in the 4f-telescope are decoupled from those introduced in the horizontal plane by the galvanometer's oscillation. Different from what is shown in Refs. [44,45], the delay introduced by our rapid delay line cannot be exclusively attributed to the displacement of the incidence point on the oscillating mirror. Instead, the whole beam path within the 4f-telescope should be considered, as demonstrated in Supplement 1 (section B).

The amplitude of the galvanometer oscillation determines the scanned delay range, and it can be adjusted simply by driving the galvanometer at a different voltage. The oscillation frequency is the device's resonant frequency, and it cannot be directly adjusted because it depends on the inertia of the oscillating part. However, the broad commercial availability of resonant scanners for laser beam deflection offers the opportunity for flexible selection of the resonant frequency, particularly in the 1-20 kHz range. This contrasts with other types of rapid scanners that would require custom manufacturing or are devoted to very different applications, which restrict the available frequencies.

Optics EXPRESS

A 1550 nm continuous-wave laser is coupled into the same delay line to track the motion of the oscillating mirror via a Mach-Zehnder interferometer (not shown in the figure).

A combination of thin and broadband quarter-waveplate and polarizer (see Fig. 1(a)) is used to efficiently pick off the delayed pulses after the second reflection on the oscillating mirror. Alternative solutions could be used to decouple the output in a purely reflective way. For example, an off-axis vertical displacement of the beam entering the 4f-telescope corresponds to an equal and opposite displacement at its exit, while maintaining its parallelism to the optic axis. We used this to separate the 1550 nm cw beam from the gate beam and record the interferogram, but the same principle could be exploited to pick off the delayed gate pulse.

The all-reflective characteristics of the delay line can, in principle, make it suitable for high-power applications, but care should be taken to avoid damaging the D-shaped retroreflector, on which the beam is focused. However, when the oscillating mirror moves, the beam focus will also scan a line across the retroreflector (see Supplement 1 Fig. S2), potentially increasing the damage threshold. In the present experiment, the pulse energy incident on the D-shaped mirror was approximately 20 nJ, with a fluence of around 1 mJ/cm^2, well below the typical damage threshold for metallic mirrors.

EOS is performed in our setup by overlapping, in time and space, the mid-IR and gate pulses, with orthogonal polarizations, in a GaSe crystal [46] with its c-axis (normal to the crystal surface) tilted in the horizontal plane to obtain birefringent phase matching. The adopted configuration (mid-IR and gate polarizations on the extraordinary and ordinary axes, respectively) generates sum-frequency components that overlap with the high-frequency portion of the non-upconverted gate spectrum but have orthogonal polarization (extraordinary). The result corresponds to a polarization change in the gate, which is measured using an ellipsometry setup [26] that inherently implements self-heterodyne balanced detection [27,28]. The ellipsometry setup comprises a short-pass filter [47], a quarter-wave plate, a Wollaston prism, and a pair of balanced InGaAs photodetectors (HBPR-200M-30K-IN, Femto Messtechnik GmbH).

The mid-IR–gate delay (EOS delay time axis) is retrieved from the interferogram of the 1550 nm beam, which is measured simultaneously with the EOS signal [48]. The interferogram and the EOS signal are recorded by a high-speed data acquisition card (GaGe Razor Express, Vitrek), with its sampling clock locked to the laser repetition rate.

As derived from the simulations in Supplement 1 (see for example the sinusoidal delay in Fig. S2 (c)), the sampling points on the EOS delay axis are non-equidistant; therefore, in order to assess the time resolution and the satisfaction of the Nyquist-Shannon sampling theorem for the mid-IR waveform sampling, we can consider the maximum delay step, which corresponds to the peak of the instantaneous frequency of the interferogram.

We can visualize the non-linear scanning as a retroreflector mounted on a translational stage moving with a sinusoidal velocity [38]. The maximum of the instantaneous frequency of the interferogram (see Fig. 1(b) top panel and Supplement 1 Fig. S1 (a)) corresponds then to the maximum scanning speed, and the corresponding delay step can be estimated by $\delta t \approx f_{\mathrm{IF}}/(f_{\mathrm{cw}} f_{\mathrm{samp}})$.

Considering a maximum instantaneous frequency of the interferogram (with $\lambda_{\mathrm{cw}} = 1.55$ μm) equal to $f_{\mathrm{IF}} = 5$ MHz (compare with Supplement 1 Fig. S1 (a)) and the sampling frequency of $f_{\mathrm{samp}} = 11$ MHz, this relation gives $\delta t \approx 2.4$ fs). The delay steps found experimentally in a single scan ranged from 0.08 to 2.6 fs. These values, well below the maximum delay step allowed by the Nyquist criterion, agree with the estimated ones and are shorter than the gate pulse duration, which is around 15 fs.

The frequency resolution is determined by the length of the scanned delay window. The delay range experimentally observed with the adopted settings was 1.2-1.4 ps and was limited by the Nyquist constraint on the maximum frequency of the interferogram (see Supplement 1 section A). Even though many fast non-repetitive dynamics involve subtle chemical shifts of narrow

Optics EXPRESS

vibrational bands, the absorption bands of biological molecules in liquid water solutions are relatively broad (10-50 cm^{-1}), and some relevant chemical dynamics can be studied, in which clearly distinct absorption bands change in amplitude. For example, the dynamics of the reactions studied in Refs. [5] and [49], involving very different time scales, would be observable even with a 28 cm^{-1} resolution. However, neither the resonant scanner delay line itself nor the laser repetition rate is an intrinsic limiting factor for the scanning window. Options are indeed available to extend it to several picoseconds without modifying the optical setup.

For example, the acquisition clock could be synchronized to a higher harmonic of the laser repetition rate. In this case, by driving the galvanometer at a higher voltage, the sampled interferogram could reach higher frequencies without aliasing, while the number of useful data points in the EOS trace would remain the same, but spread over a longer delay window (see also Supplement 1 section B). Furthermore, a different configuration, including a diffraction grating, could be adopted to introduce an additional degree of freedom for manipulating the bandwidth of the down-converted spectrum in the radio-frequency range [50]. This could allow for a more efficient use of the available Nyquist bandwidth for EOS.

The raw signals are processed using a defined workflow described in Supplement 1 (section A). A partially processed result is shown in Fig. 1(b) and (c), where the top panel shows the interferogram for delay tracking and the bottom panel displays the corresponding high-pass filtered (see Supplement 1) EOS signal given by the interaction between the gate and mid-IR pulses. The orange dots represent the symmetry points (turning points), which separate forward and backward scans. The result of the data processing is a matrix of EOS scans sharing a common linearly spaced delay axis, reconstructed from the single interferograms associated with each EOS scan. This matrix can be used to directly average EOS traces in the time domain, or compute the Fourier transform and analyze spectral information.

For comparison with a slow-scanning technique, we used a motorized translation stage to vary the length of the gate beam path. We have, in this case, modulated the mid-IR beam at 5130 Hz using a chopper wheel and a lock-in amplifier (MFLI, Zurich Instruments), with a time constant of 815.4 μs.

3. Results and discussion

Using the experimental configuration shown in Fig. 1(a), we recorded electro-optic sampling (EOS) time traces of mid-IR pulses with a resonant scanner-based rapid delay line operating at an 8 kHz scan rate. Recording both forward and backward scans results in a scan rate twice the resonant scanner frequency, which is 4 kHz. In this case, every single scan requires only 125 μs - as shown in Fig. 1(b),(c). Figure 1(d) compares a representative single scan (red line) extracted from the processed data matrix, together with the time-domain average (blue line) over 2.8 s (22618 scans).

Figure 1(d) allows a preliminary assessment of the stability of the acquisition method. Indeed, the close overlap between the integrated and single-scan traces demonstrates that averaging over multiple seconds can be performed without significant loss of information. Hence, these data confirm the mechanical stability of the resonant-scanner rapid delay line. The time-domain signal-to-noise ratio (tSNR) of the fast-scanned single EOS trace is 54 (estimated as the ratio between the average maximum of ten consecutive EOS traces and the root mean square (rms) of a single trace acquired while blocking the mid-IR beam). The shaded error bar in Fig. 1(d) represents the standard deviation of the single time traces acquired over 2.8 s. The noise on the averaged scan, considering only random fluctuations, would be given by this standard deviation, divided by the square root of the number of averaged scans. Given the tSNR of 54 on the single scan, a tSNR of around 1000 can be obtained by averaging around 350 scans (integrating over 44 ms). It should be noted that the precision on the position of the zero-crossings of the EOS scan also increases with the integration time (see also section C of Supplement 1). As a consequence,

Optics EXPRESS

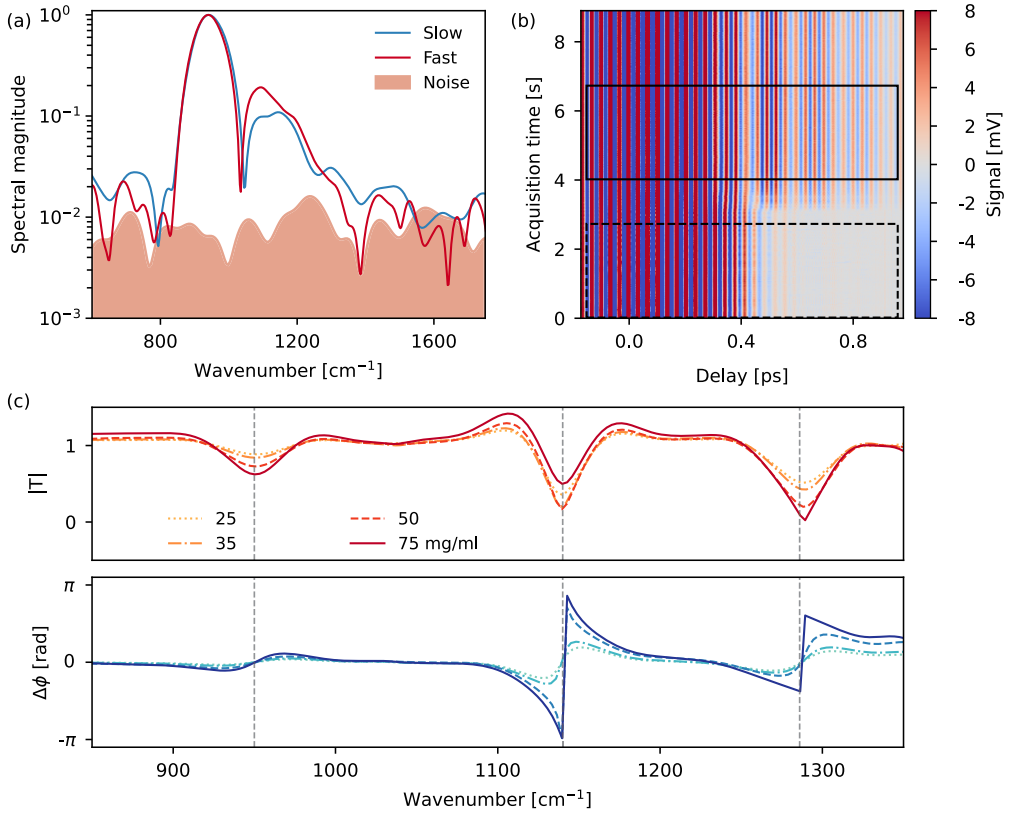

Fig. 2. (a) Comparison between the spectral magnitude of single EOS traces acquired in the same setup with a slow (blue line) and fast (red line) scanning approach. The red-shaded area represents the noise level obtained in a single fast acquisition while blocking the mid-IR beam. (b) EOS time-domain traces acquired continuously while injecting a $DMSO_2$ solution in the measurement cuvette. Reference measurement (water) is defined here (on the acquisition time axis) by the dashed rectangular box, while the equally large solid box defines the sample measurement. (c) Complex transmission function (see Eq. (1)) at four different $DMSO_2$ concentrations corresponding to the ratio of the sample and reference measurements averaged over the acquisition time intervals defined in (b). The vertical dashed lines mark the $DMSO_2$ absorption lines observed in an independent FTIR spectrum acquired in-house.

temporal shifts of the order of 1 femtosecond or lower can be detected, if necessary, by comparing the averages of multiple consecutive scans. Therefore, this technique is also suitable for retrieving complete phase information. We note here that the system's noise performance is evaluated by measuring transmission through a 30 µm water path length inside the Ge cuvette, since the target samples are water-dissolved molecules. Further quantitative assessment based on time-domain traces and considerations on the stability of our experimental setup, including Allan deviation calculations, are provided in Supplement 1 section C.

We next evaluate the accuracy of the reconstructed delay axis. To this end, it is convenient to use the frequency domain representation. Therefore, we compare the Fourier transform amplitude of a single fast scan with that obtained with a slow-scanning mechanical stage and lock-in detection. Figure 2(a) shows corresponding amplitudes of the two Fourier transforms normalized to their respective maxima. For reference, the noise floor of a single fast scan - measured with the mid-IR beam blocked, leaving only the gate beam reaching the balanced photodetectors, while

Optics EXPRESS

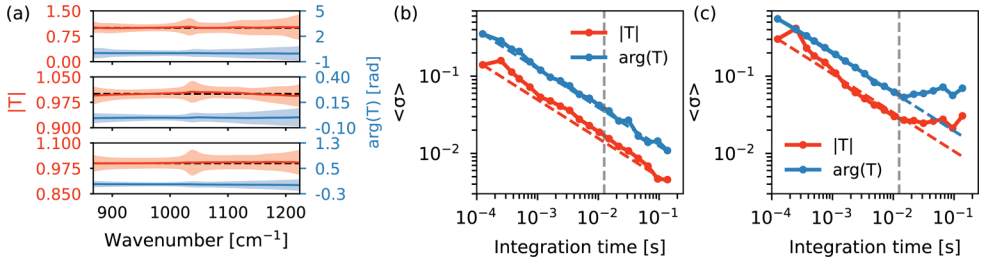

Fig. 3. (a) Mean and standard deviation of amplitude (red) and phase (blue) of identity transfer function (water/water) calculated with different modalities. Top: single transfer function as ratio of subsequent scanning cycles. Middle: ratio of the average interleaved groups, each containing 100 scans (fast referencing). Bottom: ratio of the average of subsequent non-overlapping groups of 100 scans (slow referencing). The plotted mean and standard deviations were calculated using 100 transfer functions. The horizontal dashed lines indicate the value of 1. (b)-(c) Spectrally integrated standard deviation as a function of the integration time (number of averaged scans/(8 kHz)) with the fast and slow referencing approach, respectively. The slow referencing approach is analogous to an Allan deviation. The dashed blue and red lines represent the square-root scaling ($\sim 1/\sqrt{N}$, with N number of averaged scans). The vertical dashed lines in (b) and (c) correspond to the middle and bottom panels of (a).

applying the identical acquisition and processing pipeline - is also reported in the same figure. The noise floor is also normalized to the maximum of the fast-scanned spectral amplitude.

Both spectra in Fig. 2(a) were obtained from a single scan: one was acquired in 125 µs with a data acquisition card sampling one data point per gate pulse, while the other required 3.9 s using a lock-in amplifier. The agreement supports the robustness of the retrieval algorithm based on the interferometric delay-tracking setup for reconstructing the delay axis and, consequently, providing a consistent spectrum.

To compare the noise characteristics of the resonant scanner-based delay line with those previously published using a sonotrode [40], we use the first three seconds of the acquisition of Fig. 2(b), where the sample cuvette contains only water, and the same fast referencing approach presented in Fig. 5 of Ref. [40] (explained here in Supplement 1 section D). The standard deviation of 100 single transfer functions (each one obtained using two subsequent scanning cycles) is represented by the shaded error bars in the top panel of Fig. 3(a) and corresponds to the first point (lowest integration time) in (b) (after spectral integration of the standard deviation). The mean and standard deviations in (a) are calculated using 100 single (or integrated) transfer functions. The result for the single transfer functions is one order of magnitude higher than that reported in [40]. However, the spectra obtained with the sonotrode were recorded without any sample in the beam path, whereas in the present work, the mid-IR pulses are transmitted through 30 µm of water in a Ge cuvette. The water absorption alone leads to an approximately halved EOS signal, and the inclusion of Fresnel reflections at the interfaces could give up to a five-fold total signal suppression. Since the transfer function is the ratio of two transmitted spectra, its noise depends on the relative noise of the spectra themselves. This indicates that the sonotrode setup had a better noise performance (by a factor of 2-5) compared to that presented here.

One significant contribution to this difference could be the higher operating frequency of the sonotrode-based system, which had a laser repetition rate of 28 MHz and a rapid scanning rate of 38 kHz. Other contributions could come from the additional technical differences between the two systems, for example, the different spectral coverage and balanced photodetectors model. These considerations suggest that it would be possible to achieve comparable performances under the same experimental conditions.

Optics EXPRESS

We note here that a sonotrode is a relatively bulky and costly device, typically used in industrial applications requiring high mechanical energy transfer, such as plastic welding or liquid processing, and is usually operated at vibration frequencies between 15 and 90 kHz. Given a fixed sampling frequency, which depends on the gate beam repetition rate, a high vibration frequency can produce a scanning speed that exceeds the maximum allowed by the Nyquist condition. Furthermore, integrating a sonotrode into an optical system for use as a fast delay stage requires specific modifications and handling conditions. On the other hand, resonant galvanometers are small optical components widely used for laser beam deflection, are easily mounted on an optical breadboard, are commercially available with mirrors of different sizes and coatings already mounted, and offer multiple resonant frequencies in the 1-20 kHz range. For all these reasons, a resonant scanner-based delay line can represent a more convenient choice for building a new rapid-scanning mid-IR FRS setup, depending on the specific requirements.

The middle panel of Fig. 3(a), corresponding to the vertical dashed line in (b), shows the result of the fast referencing approach with an integration time of approximately 12.5 ms. As in Ref. [40], the spectrally integrated standard deviation (Fig. 3(b)) follows the square-root dependence characteristic of white noise (demonstrated here up to an integration time of 0.15 s). The fast referencing approach effectively suppresses frequency components slower than 4 kHz, corresponding to the rate of a complete scanning cycle. On the time scale of a single scanning cycle, the measurements appear to be dominated by white noise.

To determine on which time scale correlated noise can dominate averaged measurements, we need to use a different approach, analogous to the Allan deviation and described in Supplement 1 (section C). The results are shown in Fig. 3(c), where the vertical dashed line corresponds to the bottom panel in (a). In this case, the standard deviation is larger because it does not involve the averages of two interleaved groups of scanning cycles (fast referencing approach), but the averages of subsequent non-overlapping acquisition intervals. The results show that the measurements begin to reveal correlated noise at an integration time of about 20 ms. This resembles the dependence of the slow referencing approach shown in Fig. 3 of Ref. [40] (obtained from time-domain data), where the minimum was reached around 50 ms. This means that in both the resonant scanner and the sonotrode setups, integrating consecutive scans beyond 50 ms does not improve the signal-to-noise ratio. Continuously improving noise performance for longer acquisition times has been achieved instead by using dual-oscillator systems [9,33].

To demonstrate the practical applicability of the developed resonant-scanner-based acquisition technique, we performed real-time detection of dimethyl sulfone ($DMSO_2$) dissolved in water using a flow-through cuvette (Ge windows, 30 μm path length). $DMSO_2$ was selected because it exhibits three prominent, relatively narrow absorption bands within the spectral range of our mid-IR probe pulse. $DMSO_2$ solutions (prepared in water with four concentrations: 25, 35, 50, and 75 mg/ml) were manually injected into the flow-through cuvette pre-filled with water.

The chosen concentrations exceed the typical absorption detection limits of mid-IR spectroscopy [29], because the purpose was not to optimize the sensitivity but to validate the resonant scanner approach for FRS. The sensitivity is also constrained by the cuvette's optical path length [30], which is relatively large in this case. The 30 μm path length was selected to match future microfluidic measurements of biological cells in flow, where the channel height must prevent clogging.

Figure 2(b) presents continuously acquired time-domain data during $DMSO_2$ injection. In addition to a complementary perspective on the scanning stability, the colormap reveals the onset of trailing oscillations in the wake of the pulse. These oscillations are the signature of the absorption by the vibrational modes of the $DMSO_2$. The boxes in Fig. 2(b) define the time intervals assigned to reference and sample, used in the subsequent spectral analysis.

Optics EXPRESS

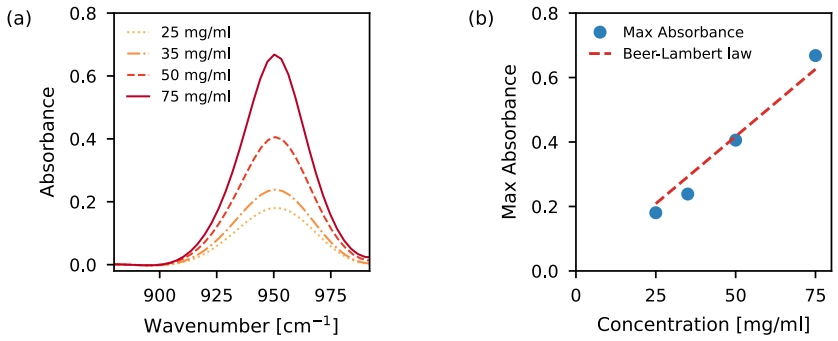

Fig. 4. (a) Absorbance peak calculated from the same data of Fig. 2(c) after setting the baseline to zero. (b) Maximum value of the absorbance peak as a function of the injected $DMSO_2$ concentration. The red dashed line is the result of a zero-intercept linear regression (Beer-Lambert law).

Figure 2(c) reports the ratio between the complex spectra obtained by computing the Fourier transforms of the sample and reference EOS scans averaged in the time domain:

$$T = \frac{E_s(\omega)e^{i\phi_s(\omega)}}{E_r(\omega)e^{i\phi_r(\omega)}} = e^{-\Delta A/2}e^{i\Delta\phi} = |T|e^{i\Delta\phi} \tag{1}$$

where $A_{s(r)} = -2\log(E_{s(r)}/E_0)$ defines a sample and reference absorbance (with E_0 representing the incident field), and their difference $\Delta A = A_s - A_r$ is the actual measured absorbance. A factor of 2 is used because T is defined here as the ratio of electric-field amplitudes rather than intensities. The three absorption bands of $DMSO_2$ appear as minima in the transmission amplitude, accompanied by corresponding inflection points of the phase, in agreement with Kramers-Krönig relations. In addition to the $DMSO_2$ signatures, we observe a modulation in the baseline, which we attribute to incomplete cancellation of the broad water absorption bands at high sample concentration and to changes in water structure arising from the hydration shell formed by dissolved $DMSO_2$ molecules. Given the dependence on ΔA (see Eq. (1)), a change in the solvent can appear as a $|T|$ higher than 1. This explanation is supported by the fact that the deviations of the transmittance baseline from 1 increase with the sample concentration. Additional contributions to a distorted absorption line shape could also come from beam pointing fluctuations introduced by the scanning mirror (see also section A of Supplement 1). However, these distortions may not hinder an accurate measurement of relative changes when monitoring dynamical processes.

Quantitative concentration information can be extracted, for example, from the absorption peak at the lowest wavenumber, as shown in Fig. 4. The transmission can be converted to absorbance using $\Delta A = -2\log|T|$. A simple baseline correction is applied, subtracting the average absorbance over a short range just before the peak. A zero-intercept line (Beer-Lambert law) is used to fit the measured absorbance maxima as a function of the concentration and is drawn in Fig. 4(b) for comparison with the data.

The main outcome of the $DMSO_2$ measurements is to demonstrate the possibility of referencing with respect to the solvent absorption spectrum on a time scale of a few seconds or lower. This can be essential for suppressing distortion caused by laser fluctuations. While manual injection limits the sample-reference modulation period to a few seconds, integration with automated microfluidics would allow much faster alternation, fully exploiting the advantage of a kHz-scan rate [9].

Optics EXPRESS

4. Conclusion

We demonstrated electro-optic sampling of mid-infrared pulses using a resonant galvanometer–based rapid delay line. The system achieves a full-waveform acquisition rate of 8 kHz, with a compact design based on a single laser oscillator. We further validated the approach through real-time, solvent-referenced detection of a model molecule dissolved in water in a flow-through cuvette. These results establish resonant-scanner-based EOS as a simple, cost-effective platform for high-speed field-resolved infrared spectroscopy in dynamic aqueous environments.

Future improvements will open new possibilities for advancing the applications of infrared FRS, including high-throughput chemical fingerprinting, label-free flow cytometry, environmental monitoring, and the study of fast, non-repetitive dynamics.

Funding. Ludwig-Maximilians-Universität München; Max-Planck-Gesellschaft; Max Planck Institute of Quantum Optics; Ministry of Culture and Innovation of Hungary (2020-2.1.1-ED-2022-00213); Bavarian State Ministry for Science and Art; Research Center OPTIMAS; European Research Council (101088303); Fraunhofer-Max-Planck Cooperation Programme (iFRS).

Acknowledgment. The authors would like to thank Bojan Resan for the insightful and constructive discussions and feedback during his stay with the BIRD team.

Disclosures. The authors declare no conflicts of interest.

Data availability. Data underlying the results presented in this paper are not publicly available at this time but may be obtained from the authors upon reasonable request.

Supplemental document. See Supplement 1 for supporting content.

References

1. W. Uhmann, A. Becker, C. Taran, *et al.*, "Time-resolved FT-IR absorption spectroscopy using a step-scan interferometer," Appl. Spectrosc. **45**(3), 390–397 (1991).
2. K. Gerwert, "Molecular reaction mechanisms of proteins as monitored by time-resolved FTIR spectroscopy," Curr. Opin. Struct. Biol. **3**(5), 769–773 (1993).
3. C. J. Manning, "Smoke and mirrors: Ultra-rapid-scan FT-IR spectrometry," in *Fourier Transform Spectroscopy: 11th International Conference* (AIP, 1998), pp. 84–95.
4. J. L. Klocke, M. Mangold, P. Allmendinger, *et al.*, "Single-shot sub-microsecond mid-infrared spectroscopy on protein reactions with quantum cascade laser frequency combs," Anal. Chem. **90**(17), 10494–10500 (2018).
5. M. J. Norahan, R. Horvath, N. Woitzik, *et al.*, "Microsecond-resolved infrared spectroscopy on nonrepetitive protein reactions by applying caged compounds and quantum cascade laser frequency combs," Anal. Chem. **93**(17), 6779–6783 (2021).
6. N. Nitta, T. Iino, A. Isozaki, *et al.*, "Raman image-activated cell sorting," Nat. Commun. **11**(1), 3452 (2020).
7. K. Hiramatsu, T. Ideguchi, Y. Yonamine, *et al.*, "High-throughput label-free molecular fingerprinting flow cytometry," Sci. Adv. **5**(1), eaau0241 (2019).
8. D. Gerz, M. Huber, H. Mirkes, *et al.*, "High-speed field-resolved infrared fingerprinting of particles in flow," in *Conference on Lasers and Electro-Optics Europe & European Quantum Electronics Conference* (IEEE, 2023), p. 1.
9. W. Schweinberger, S. Gröbmeyer, A. Chamankar, *et al.*, "Field-resolved sample-modulation spectroscopy for mid-infrared molecular fingerprinting," in *Conference on Lasers and Electro-Optics Europe & European Quantum Electronics Conference* (2025), p. 1.
10. J. Haas and B. Mizaikoff, "Advances in mid-infrared spectroscopy for chemical analysis," Annu. Rev. Anal. Chem. **9**(1), 45–68 (2016).
11. M. Liu, R. M. Gray, L. Costa, *et al.*, "Mid-infrared cross-comb spectroscopy," Nat. Commun. **14**(1), 1044 (2023).
12. P. A. Elzinga, F. E. Lytle, Y. Jian, *et al.*, "Pump/probe spectroscopy by asynchronous optical sampling," Appl. Spectrosc. **41**(1), 2–4 (1987).
13. A. Schliesser, N. Picqué, and T. W. Hänsch, "Mid-infrared frequency combs," Nat. Photonics **6**(7), 440–449 (2012).
14. I. Coddington, N. Newbury, and W. Swann, "Dual-comb spectroscopy," Optica **3**(4), 414 (2016).
15. Y. Jin, S. M. Cristescu, F. J. M. Harren, *et al.*, "Two-crystal mid-infrared optical parametric oscillator for absorption and dispersion dual-comb spectroscopy," Opt. Lett. **39**(11), 3270 (2014).
16. N. S. Han, J. Kim, T. H. Yoon, *et al.*, "Broadband infrared spectroscopy of molecules in solutions with two intrapulse difference-frequency-generated mid-infrared frequency combs," J. Phys. Chem. B **125**(1), 307–316 (2021).
17. S. Vasilyev, A. Muraviev, D. Konnov, *et al.*, "Longwave infrared (6.6-11.4 μm) dual-comb spectroscopy with 240,000 comb-mode-resolved data points at video rate," Opt. Lett. **48**(9), 2273–2276 (2023).
18. M. Yu, Y. Okawachi, A. G. Griffith, *et al.*, "Silicon-chip-based mid-infrared dual-comb spectroscopy," Nat. Commun. **9**(1), 1869 (2018).
19. E. Lins, S. Read, B. Unni, *et al.*, "Microsecond resolved infrared spectroelectrochemistry using dual frequency comb ir lasers," Anal. Chem. **92**(9), 6241–6244 (2020).

Optics EXPRESS

20. F. Tauser, C. Rausch, J. H. Posthumus, *et al.*, "Electronically controlled optical sampling using 100 MHz repetition rate fiber lasers," in *Commercial and Biomedical Applications of Ultrafast Lasers VIII*, vol. 6881 (SPIE, 2008), p. 68810O.
21. S. M. M. Friis and L. Høgstedt, "Upconversion-based mid-infrared spectrometer using intra-cavity LiNbO3 crystals with chirped poling structure," Opt. Lett. **44**(17), 4231 (2019).
22. K. Hashimoto, T. Nakamura, T. Kageyama, *et al.*, "Upconversion time-stretch infrared spectroscopy," Light: Sci. Appl. **12**(1), 48 (2023).
23. A. Kawai, K. Hashimoto, T. Dougakiuchi, *et al.*, "Time-stretch infrared spectroscopy," Commun. Phys. **3**(1), 152 (2020).
24. A. Dabrowska, M. David, S. Freitag, *et al.*, "Broadband laser-based mid-infrared spectroscopy employing a quantum cascade detector for milk protein analysis," Sens. Actuators, B **350**, 130873 (2022).
25. J. A. Valdmanis, G. Mourou, and C. W. Gabel, "Picosecond electro-optic sampling system," Appl. Phys. Lett. **41**(3), 211–212 (1982).
26. G. Gallot and D. Grischkowsky, "Electro-optic detection of terahertz radiation," J. Opt. Soc. Am. B **16**(8), 1204–1212 (1999).
27. I.-C. Benea-Chelmus, J. Faist, A. Leitenstorfer, *et al.*, "Electro-optic sampling of classical and quantum light," Optica **12**(4), 546 (2025).
28. C. Hofer, D. Bausch, L. Fürst, *et al.*, "Linear field-resolved spectroscopy approaching ultimate detection sensitivity," Opt. Express **33**(1), 1–17 (2025).
29. I. Pupeza, M. Huber, M. Trubetskov, *et al.*, "Field-resolved infrared spectroscopy of biological systems," Nature **577**(7788), 52–59 (2020).
30. M. Huber, M. Trubetskov, S. A. Hussain, *et al.*, "Optimum sample thickness for trace analyte detection with field-resolved infrared spectroscopy," Anal. Chem. **92**(11), 7508–7514 (2020).
31. D. C. Edelstein, R. B. Romney, and M. Scheuermann, "Rapid programmable 300 ps optical delay scanner and signal-averaging system for ultrafast measurements," Rev. Sci. Instrum. **62**(3), 579–583 (1991).
32. A. S. Kowligy, H. Timmers, A. J. Lind, *et al.*, "Infrared electric field sampled frequency comb spectroscopy," Sci. Adv. **5**(6), eaaw8794 (2019).
33. A. Weigel, P. Jacob, W. Schweinberger, *et al.*, "Dual-oscillator infrared electro-optic sampling with attosecond precision," Optica **11**(5), 726 (2024).
34. S. M. Teo, B. K. Ofori-Okai, C. A. Werley, *et al.*, "Invited article: Single-shot THz detection techniques optimized for multidimensional thz spectroscopy," Rev. Sci. Instrum. **86**(5), 051301 (2015).
35. M. E. Kozina and M. C. Hoffmann, "Single-shot electro-optic measurement of mid-infrared pulses," in *Conference on Lasers and Electro-Optics* (Optica Publishing Group, 2018), paper SM4A.6.
36. Y. Nomura, Y.-T. Wang, T. Kozai, *et al.*, "Single-shot detection of mid-infrared spectra by chirped-pulse upconversion with four-wave difference frequency generation in gases," Opt. Express **21**(15), 18249–18254 (2013).
37. B. Urbanek, M. Möller, M. Eisele, *et al.*, "Femtosecond terahertz time-domain spectroscopy at 36 kHz scan rate using an acousto-optic delay," Appl. Phys. Lett. **108**(12), 121101 (2016).
38. T. Vogel and C. J. Saraceno, "Advanced data processing of THz-time domain spectroscopy data with sinusoidally moving delay lines," J. Infrared, Millimeter, Terahertz Waves **45**(11-12), 967–983 (2024).
39. B. Süss, F. Ringleb, and J. Heberle, "New ultrarapid-scanning interferometer for FT-IR spectroscopy with microsecond time-resolution," Rev. Sci. Instrum. **87**(6), 063113 (2016).
40. A. Weigel, P. Jacob, D. Gröters, *et al.*, "Ultra-rapid electro-optic sampling of octave-spanning mid-infrared waveforms," Opt. Express **29**(13), 20747 (2021).
41. G. J. Kim, S. G. Jeon, J. I. Kim, *et al.*, "Terahertz pulse detection using rotary optical delay line," Jpn. J. Appl. Physics, Part 1: Regul. Pap. Short Notes Rev. Pap. **46**(11R), 7332–7335 (2007).
42. H. Guerboukha, A. Markov, H. Qu, *et al.*, "Time resolved dynamic measurements at THz frequencies using a rotary optical delay line," IEEE Trans. Terahertz Sci. Technol. **5**(4), 564–572 (2015).
43. R. Fleddermann, W. M. Lee, K. Huang, *et al.*, "Compact flexible multi-pass rotary delay line using spinning micro-machined mirrors," Sci. Rep. **7**(1), 9299 (2017).
44. X. Liu, M. J. Cobb, and X. Li, "Rapid scanning all-reflective optical delay line for real-time optical coherence tomography," Opt. Lett. **29**(1), 80–82 (2004).
45. K. Hashimoto, M. Takahashi, T. Ideguchi, *et al.*, "Broadband coherent raman spectroscopy running at 24,000 spectra per second," Sci. Rep. **6**(1), 21036 (2016).
46. K. Liu, J. Xu, and X. C. Zhang, "GaSe crystals for broadband terahertz wave detection," Appl. Phys. Lett. **85**(6), 863–865 (2004).
47. M. Porer, J.-M. Ménard, and R. Huber, "Shot noise reduced terahertz detection via spectrally postfiltered electro-optic sampling," Opt. Lett. **39**(8), 2435 (2014).
48. W. Schweinberger, L. Vamos, J. Xu, *et al.*, "Interferometric delay tracking for low-noise Mach-Zehnder-type scanning measurements," Opt. Express **27**(4), 4789 (2019).
49. A. Schwaighofer, C. K. Akhgar, and B. Lendl, "Broadband laser-based mid-ir spectroscopy for analysis of proteins and monitoring of enzyme activity," Spectrochim. Acta, Part A **253**, 119563 (2021).
50. K. Hashimoto and T. Ideguchi, "Phase-controlled fourier-transform spectroscopy," Nat. Commun. **9**(1), 4448 (2018).